ELSEVIER

First use of an airborne thermal infrared hyperspectral scanner for compositional mapping

Laurel Kirkland[a,b,*], Kenneth Herr[c], Eric Keim[c], Paul Adams[c], John Salisbury[d,1], John Hackwell[c], Allan Treiman[a]

[a]*Lunar and Planetary Institute, 3600 Bay Area Boulevard, Houston, TX 77058-1113, USA*
[b]*The Aerospace Corporation, Houston, TX, USA*
[c]*The Aerospace Corporation, P.O. Box 92957, Los Angeles, CA 90009-2957, USA*
[d]*Johns Hopkins University, 84 Cochise Street, Palm Coast, FL 32137, USA*

Abstract

In May 1999, the airborne thermal infrared hyperspectral imaging system, Spatially Enhanced Broadband Array Spectrograph System (SEBASS), was flown over Mormon Mesa, NV, to provide the first test of such a system for geological mapping. Several types of carbonate deposits were identified using the 11.25-μm band. However, massive calcrete outcrops exhibited weak spectral contrast, which was confirmed by field and laboratory measurements. Because the weathered calcrete surface appeared relatively smooth in hand specimen, this weak spectral contrast was unexpected. Here we show that microscopic roughness not readily apparent to the eye has introduced both a cavity effect and volume scattering to reduce spectral contrast. The macroroughness of crevices and cobbles may also have a significant cavity effect. The diminished spectral contrast is important because it places higher signal-to-noise ratio (SNR) requirements for spectroscopic detection and identification. This effect should be factored into instrumentation planning and interpretations, especially interpretations without benefit of ground truth. SEBASS had the required high SNR and spectral resolution to allow us to demonstrate for the first time the ability of an airborne hyperspectral thermal infrared scanner to detect and identify spectrally subtle materials. © 2002 Elsevier Science Inc. All rights reserved.

1. Introduction

The ~8- to 12-μm atmospheric window has been used in numerous remote sensing studies to map variations in surface composition. Kahle, Palluconi, and Christensen (1993) and Hook, Abbott, Grove, Kahle, and Palluconi (1999) present good reviews. The 8- to 12-μm region includes intense molecular vibration bands of silicates, and also characteristic bands of other minerals, including carbonates (e.g., Lyon, 1963; Salisbury, Walter, Vergo, & D'Aria, 1991).

Almost all airborne terrestrial thermal infrared studies have focused on multichannel radiometer (multispectral) data sets, typically with 4–10 bands. In one of the earliest studies, Vincent and Thomson (1972) and Vincent, Thomson, and Watson (1972) used an imaging two-band radiometer to show that quartz-rich regions can be differentiated from regions that lack silicates, based on ratios of an 8.2- to 10.9-μm band to a 9.4- to 12.1-μm band. Their work demonstrated both the utility of an imaging instrument and the advantages of the strong silicate band for remote sensing. Kahle and Rowan (1980) investigated this approach in more detail using a six-band, 8.3- to 13-μm range radiometer. They used statistical techniques to define type regions, and then identified materials using ground truth.

These were followed by numerous studies using imaging multichannel radiometers, and similar statistical techniques to define type units, which were then identified with ground truth. Representative instruments include the Thermal Infrared Multispectral Scanner (TIMS) (Abrams,

* Corresponding author. Lunar and Planetary Institute, 3600 Bay Area Boulevard, Houston, TX 77058-1113, USA.
E-mail addresses: kirkland@lpi.usra.edu (L. Kirkland), kenneth.c.herr@aero.org (K. Herr), eric.r.keim@aero.org (E. Keim), paul.m.adams@aero.org (P. Adams), salisburys@worldnet.att.net (J. Salisbury), john.a.hackwell@aero.org (J. Hackwell), treiman@lpi.usra.edu (A. Treiman).
[1] Retired.

Abbott, & Kahle, 1991; Gillespie, Kahle, & Palluconi, 1984; Kahle & Goetz, 1983), the Moderate Resolution Imaging Spectroradiometer (MODIS) Airborne Simulator (MAS) (King et al., 1996), and, on the Terra satellite, the MODIS (Barnes, Pagano, & Salomonson, 1998) and the Advanced Spaceborne Thermal Emission and Reflection Radiometer (ASTER) (Fujisada & Ono, 1991).

In remote sensing studies, it is important to note the difference among detection, discrimination, and identification. *Detection* requires a spectral signal that rises to a statistically meaningful level above the noise level; *discrimination* requires the spectral signal be detectable and also different from the surrounding materials; and *identification* requires both discrimination and a spectral band shape that can be considered unambiguous and that can be converted to an appropriate unit for comparison to laboratory measurements. For example, remotely sensed spectra may be converted to apparent emissivity and compared to laboratory spectra scaled in emissivity (Kahle & Alley, 1992). Emissivity is the measured radiance divided by the blackbody radiance at the target kinetic temperature. When the true target temperature is not known, it must be estimated, and apparent emissivity is the measured radiance divided by the blackbody radiance calculated at the estimated target temperature (Conel, 1969).

The ability of any spectral instrument to detect and uniquely identify surface minerals is proportional to the strength, width, and number of bands exhibited by the mineral over the spectral range measured; confidence in identification is also increased by the instrument calibration, atmospheric compensation, and conversion to a unit for comparison to laboratory spectra; and the information content of each spectrum. Information content increases with higher spectral resolution, signal-to-noise ratio (SNR), spectral range, and denser sampling interval (Kirkland et al., 2001). The difficulty of unique identification is also increased by surface weathering and roughness, and the number of endmembers and range of particle sizes present.

Thermal infrared remote sensing studies of Earth's surface have generally used multiband radiometers rather than spectrometers. A search of the literature returned no peer-reviewed studies that made extensive use of airborne thermal infrared imaging spectrometer data. In part, this results from the high data rate required of an imaging spectrometer, the lower SNR that results from narrower bands, and the ability to combine statistical differentiation of type regions with ground truth to identify the minerals present. An important drawback inherent in using less than ~10 bands is that surface components other than quartz commonly cannot be uniquely identified without ground truth (Crowley & Hook, 1996).

However, under some conditions, materials with narrow or weak features may be differentiated from those that have strong features. For example, several studies have focused on discriminating between silicate signatures, or between silicates and nonsilicates. Targets that lack a clearly detect-

able spectral feature in imagery collected from a multi-channel instrument are frequently differentiated statistically from the surrounding regions, based on an overall difference in emissivity or continuum, the lack of a silicate feature, or broad inflections that are not uniquely diagnostic, and then the targets are subsequently identified using ground truth (e.g., Crowley & Hook, 1996; Gillespie, 1992; Gillespie et al., 1984; Gillespie, Kahle, & Walker, 1986; Kahle & Rowan, 1980).

For this study, we desired to assess how well and under what conditions carbonates may be detected, and under what conditions they may be identified using remotely sensed thermal infrared spectra, with a specific focus on the conditions and instrumentation required to detect and identify carbonates without benefit of ground truth. As noted above, the ability to detect a mineral is proportional to the exhibited spectral band strengths. Weathering, surface roughness, and the presence of small particles can dramatically reduce the band contrast of most materials, including calcite (Hunt & Logan, 1972; Lyon, 1964; Salisbury, Hapke, & Eastes, 1987; Salisbury & Wald, 1992). Proper interpretation of remotely sensed signatures requires consideration of the effects of grain size, surface roughness, and surface weathering on the observed spectrum.

In the thermal infrared, calcite has clearly discernable bands centered near 6.5, 11.2, and 33 μm. Our field work focuses on the 11.2-μm band because it falls within the terrestrial atmospheric ~8- to 12-μm window, but our laboratory studies include an examination of the 6.5- and 33-μm bands for completeness. Since the 11.2-μm carbonate band is generally too narrow and weak to be detected and identified by a multichannel radiometer, we utilized data collected by the hyperspectral imaging spectrometer Spatially Enhanced Broadband Array Spectrograph System (SEBASS) (Hackwell et al., 1996).

2. Background: variations in band strengths

Laboratory spectra measured of large-grained, smooth-surfaced, high-purity minerals are frequently used to predict the spectral contrast that will be recorded by a remote sensing instrument (Christensen et al., 2000; Lane & Christensen, 1997). For example, the limestone hand sample spectrum in Fig. 1 exhibits a band contrast of ~15% at 11.25 μm and 35% at ~6.5 μm. The spectrum was measured in hemispherical reflectance and converted to emissivity using 1 − reflectance (Kirchhoff's Law, Nicodemus, 1965). Calcite spectra published by Lane and Christensen (1997) exhibit band contrasts ranging from ~20% to 40% at ~11.2 μm and from ~30% to 80% at ~6.5 μm. These band contrasts may be used to calculate the minimum area coverage required by the mineral for detection.

However, early workers noted that spectral contrast varies with sample condition. Lyon (1963, 1964) first found that spectral contrast of mineral and rock spectra decreased

with decreasing particle size—an effect described and variously explained repeatedly since that time (e.g., Aronson, Emslie, & McLinden, 1966; Conel, 1969; Hunt & Logan, 1972; Salisbury et al., 1987; Salisbury & Wald, 1992; Vincent & Hunt, 1968). Spectra of vesicular rocks and rough lava flows have also been shown to have low spectral contrast (Kahle et al., 1988; Ramsey & Fink, 1999) In order to understand these observations, it is critical to consider two important surface property effects that affect spectral contrast—volume scattering and the cavity effect.

2.1. Surface and volume scattering

As first described for mineral samples by Vincent and Hunt (1968), light can be scattered by a material by two processes—surface and volume scattering. A strong band is produced by a Fresnel reflection from the surface (surface scattering) because high opacity within the band gives it a mirror-like property. This mirror-like reflectance produces reflectance peaks called "reststrahlen bands." In the case of emission, "strictly speaking, the surface of a body never emits rays, but rather it allows part of the rays coming from the interior to pass through. The other part is reflected inward and according(sic) as the fraction transmitted is larger or smaller, the surface seems to emit more or less intense radiation" (Planck, 1914; see also Hunt & Vincent, 1968). Thus, reststrahlen reflectance at the internal surface of the grain reduces emerging radiation at the reststrahlen feature, resulting in an emissivity trough (Figs. 1 and 2). Surface scattering depends on both the real and imaginary indices of the refractive index (Salisbury et al., 1987; Vincent & Hunt, 1968).

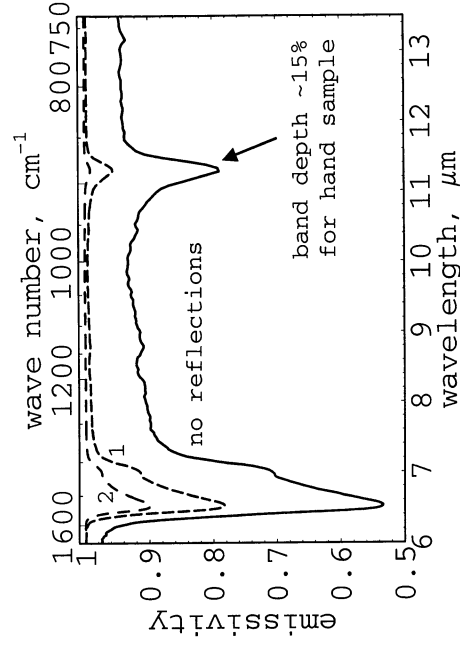On the other hand, lower opacity provides an opportunity for internal (volume) scattering. Pure volume scattering depends only on the imaginary index of refraction. In reflectance, reflected radiation passes through optically thin particles, imposing a transmission spectrum on the scattered radiation. In emission, optically thin single particles preferentially emit where they absorb (Hunt & Logan, 1972), resulting in emissivity peaks given by emissivity=1−transmission, as illustrated in Fig. 2.

Since spectral features dominated by surface scattering appear as emission troughs, while features dominated by volume scattering appear as emission peaks shifted slightly to longer wavelength, both band strength and band shape vary with the relative contribution from each process. Reststrahlen bands of large, optically thick particles are dominated by surface scattering. Vincent and Hunt (1968) showed that as a mineral is ground up, the particles may become optically thin, so volume scattering has a greater effect, and the spectral shape begins to shift more towards the shape of a pure volume scattering spectrum (Fig. 2). As the contribution from volume scattering increases, the reststrahlen band shape changes and shifts to longer wavelength, and loses spectral contrast and then inverts, as illustrated in Fig. 2.

A smooth surface enhances a strong Fresnel reflection (surface scattering). However, microscopic surface asperities (walls of pits or projecting thin edges or grains) may be optically thin, and result in volume scattering (Aronson et al., 1966; Salisbury & Wald, 1992). Also, surface texture (roughness) can produce a cavity effect that can introduce effects similar to particle size.

2.2. Cavity effect

The cavity (hohlraum) effect results from multiple surface scattering reflections from internal cavity surfaces, which reduces the spectral contrast. The effective emissivity
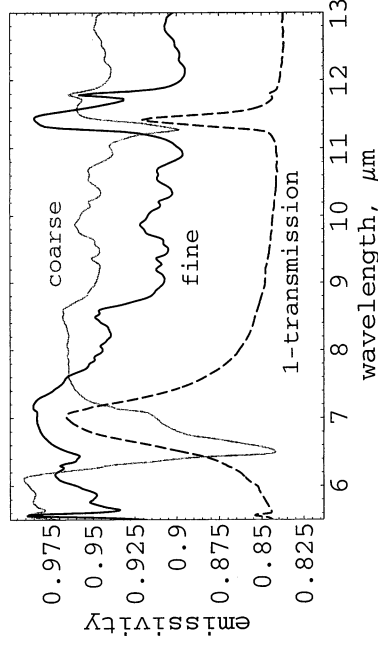

Fig. 2. Surface and volume scattering. The dashed line shows a transmission spectrum of calcite, and the black and gray traces are biconical reflectance spectra of fine and coarse calcite particles (0–74 and 74–250 μm, respectively). Surface scattering dominates for the coarse particles, while volume scattering dominates the transmission spectrum, and a combination occurs in the fine calcite spectrum. Spectra from Salisbury et al. (1991) of their sample labeled "calcite.1," converted to emissivity using 1−reflectance (or transmission), with transmission scaled to plot in a convenient range for display.

Fig. 1. Carbonate band contrast. The lower trace shows a limestone spectrum of a hand sample, which exhibits a typical 11.25-μm band depth for massive carbonate. The middle and upper traces show the calculated effective emissivity that results from the cavity effect for one and two reflections, respectively, using Eq. (1).

varies with the number of times the energy is reflected, and is given by (Fraden, 1993):

$$\varepsilon_e = 1 - (1 - \varepsilon)^{(count+1)} \tag{1}$$

where ε_e = the effective emissivity; ε = the emissivity of the cavity wall; and count = the number of times the energy is reflected.

With increasing number of reflections, the emissivity increases at all wavelengths and the spectral contrast decreases (Fig. 1). Thus, lower spectral band contrast will result from the presence of a rough, pitted surface, vesicles, pits such as those that occur between particles of sand or pebbles, or crevasses between boulders. For example, Kahle et al. (1988) and Ramsey and Fink (1999) note that the cavity effect will reduce spectral contrast in vesicular basalt. However, this effect has not previously been noted in remote sensing studies of nonvesicular materials.

In general, the greater the ratio of the cavity depth to entrance width, the greater the cavity effect (Williams & Becklund, 1984). However, determining the number of reflections even for simple shapes, such as cylinders and cones, is a very complex problem, and is a function of the cavity shape, cavity area, entrance aperture area, the emissivity of the cavity wall, and whether the wall reflects diffusely or specularly (Bartell, 1981; LaRocca, 1978; Williams & Becklund, 1984). Nonetheless, it is obvious that increasing surface roughness is likely to increase the number of multiple reflections, resulting in decreased spectral contrast of reststrahlen bands. On the other hand, it is not generally appreciated that these effects occur for roughness down to a scale of at least ~ 1/5 the wavelength (Siegel & Howell, 1968), nor, in the other direction, that macroroughness formed by cobbles and boulders will also introduce a cavity effect.

Fig. 3. Mormon Mesa and field spectrometer van. The indurated calcite (calcrete) cap rock is visible along the cliff edge (left), and extensive coverage of calcrete fragments is visible on the mesa top, over a reddish quartz and calcite soil.

Fig. 4. Typical calcrete sample, collected with the in situ top surface marked for reference. Larger divisions of ruler are centimeters.

Thus, both volume scattering and the cavity effect reduce the spectral contrast of reststrahlen bands. However, the cavity effect increases the emissivity at all wavelengths (Fig. 1), while volume scattering increases the emissivity within the reststrahlen bands, but decreases the emissivity at other wavelengths (Fig. 2).

3. Field site

The Mormon Mesa site studied is approximately 6 miles west of Mesquite, NV (latitude 36°45', longitude 114°15'). Gardner (1968, 1972) give extensive geologic descriptions of the region. Carbonate is found there in four broad categories: (1) strongly indurated, massive carbonate (calcrete) (Figs. 3–4); (2) limestone in the asphalt road aggregate (Fig. 5); (3) limestone cobbles in a conglomerate with an indurated carbonate matrix that occurs in localized drainage regions (Fig. 6); and (4) fine particulate calcite in the reddish mesa soil.
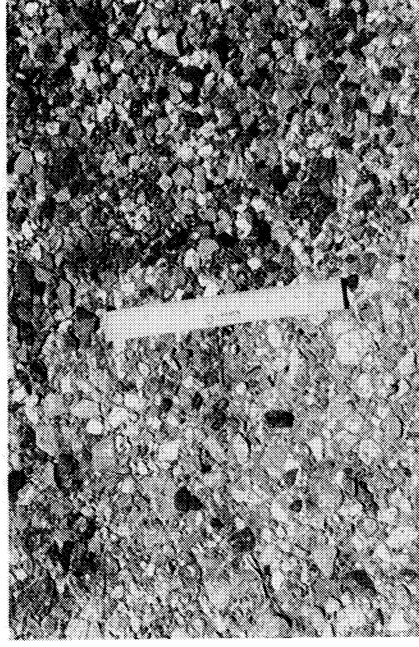

Fig. 5. Asphalt road. The brighter aggregate in the left of the image contains limestone and silicates, while the darker aggregate to the right is composed mainly of silicates. The ruler is ~ 17 cm long.
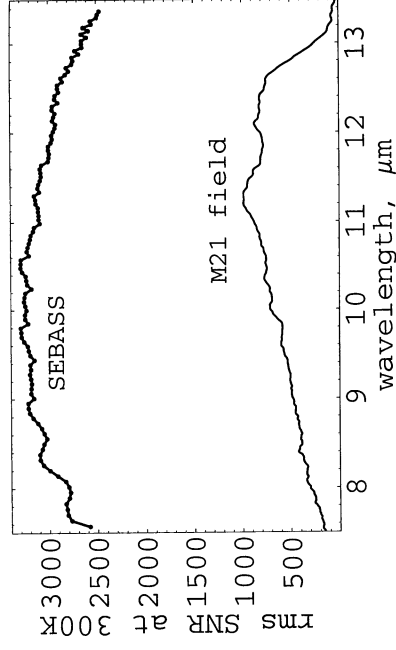
Fig. 7. SEBASS and field spectrometer SNR. The upper trace shows the rms SNR for a single spectrum of a blackbody at 300 K for SEBASS, and the lower trace for the M21 field spectrometer. Higher numbers represent greater sensitivity.

4. Data

We measured hyperspectral data from three perspectives: airborne (SEBASS), in situ (field spectrometers), and laboratory reflectance spectra. The Aerospace Corporation operates SEBASS, the field spectrometers, and the laboratory equipment. Aerospace is a nonprofit Federally Funded Research and Development Center (FFRDC) that specializes in the development and assessment of advanced technology. SEBASS is operated by the Office of Spectral Applications, the field spectrometers by the Surveillance Technologies Department, and the laboratory equipment by the Materials Processing and Evaluation Department.

4.1. SEBASS

The SEBASS is a liquid helium cooled prism spectrometer that measures the two mid-infrared terrestrial transmission "windows" in the wavelength ranges 2.42–5.33 μm (4132–1876 cm^{-1}) and 7.57–13.52 μm (1321–740 cm^{-1}) (Table 1). Each range is measured in 128 channels, with a spectral resolution of 0.088 μm (7 cm^{-1}) at 11.25 μm (890 cm^{-1}), defined as two times the sampling interval. SEBASS has a 1-mrad field-of-view per pixel, and operates as a pushbroom instrument, using two 128 × 128 detector arrays. The entire optical bench is cooled to 4 K using liquid helium to allow the use of a more sensitive detector and to increase the SNR (Hackwell et al., 1996). Here we use the long wavelength hyperspectral images that are 128 pixels wide and 2000 pixels long, measured with a spatial resolution of ~2 × 2 m. We chose the Mormon Mesa as a carbonate-rich study region, where the SEBASS team could simultaneously perform a georeferencing demonstration and also provide a unique data set to help further the community's understanding of spectral variations exhibited by field materials.

Fig. 7 shows the SEBASS root mean square (rms)

SNR. For SEBASS, the rms SNR is ~4.8 times greater than the peak-to-peak SNR, which is typical for an instrument dominated by random noise (Griffiths & de Haseth, 1986). The peak-to-peak noise is the difference between the maximum and minimum values measured at a given wavelength using multiple measurements of the same target, such as the calibration blackbody (Kirkland et al., 2001). The rms noise is the standard deviation of multiple measurements at a given wavelength of the same target (Ingle & Crouch, 1998). SEBASS measures with the highest combined spectral resolution and SNR of any terrestrial airborne imaging thermal infrared spectrometer, and therefore is uniquely able to detect and examine the diagnostic signatures of spectrally subtle materials.

SEBASS spectra were processed as follows.

(1) Spectra were calibrated by the SEBASS team to radiance using two onboard blackbody targets.

(2) To compensate atmospheric spectral features, we applied an In-Scene Atmospheric Compensation (ISAC) that the SEBASS team developed (Johnson, 1998; Kaiser, 1999; Young, 1998). ISAC is based on the assumption that for a given wavelength, there are measurements within the scene of a material with an emissivity of one at the chosen wavelength. Commonly, the high emissivity material is vegetation or water, or minerals for wavelengths outside of characteristic bands. For example, quartz has an emissivity peak at 12.2 μm due to a secondary Christiansen feature. ISAC does not require the material to be a blackbody at all wavelengths, nor does ISAC require running a radiative transfer model such as MODTRAN. ISAC compensates for atmospheric transmission and upwelling radiance, but not for the effects of reflected downwelling radiance.

We apply ISAC in three steps. First, we calculate the wavelength that most often exhibits the maximum brightness temperature, and set this as the reference wavelength. Only spectra that have their highest brightness temperature at this wavelength are used to calculate the atmospheric
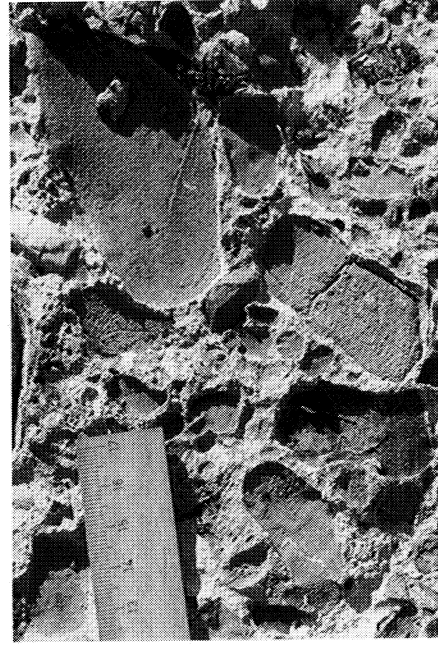

Fig. 6. Arroyo conglomerate. The conglomerate consists mainly of limestone cobbles in a matrix of indurated calcite, with some sandstone cobbles. Larger divisions of the ruler are centimeters.

Table 1
Field instrument parameters

	SEBASS	M21
11 μm signal-to-noise ratio[a]	3098	944[b]
9 μm spectral resolution (cm^{-1})	13.7	3.4[c]
11 μm spectral resolution (cm^{-1})	7.4	3.4[c]
13 μm spectral resolution (cm^{-1})	4.4	3.4[c]
field of view (milliradian)	1	8
pixel size (m)	~2×2	~0.3×~0.3[d]
bands/spectrum	128	1024
wavelength range (μm)	7.57–13.52	6.68–14.28

[a] rms signal to noise ratio for blackbody at 300 K.
[b] Value for a single spectrum, and averages of ~15–20 spectra were used to increase the SNR.
[c] Apodized spectral resolution.
[d] Pixel size at ~30 m, which was a typical distance.

compensation. Second, for each wavelength, we make a scatterplot using as x-values the reference radiance scaled to the blackbody radiance at the chosen wavelength, and y-values are the measured radiance at the chosen wavelength. We then fit a line to the highest points that occur along the scatterplot (Fig. 8), and weight the fit to assign more weight to regions with denser sampling. This fit is then offset to account for the bias introduced by noise (Johnson, 1998; Young, 1998). Third, we apply the atmospheric compensation using the slope and offset calculated for the line fit, so that (Eq. (2)):

$$radiance_{compensated} = \frac{radiance_{uncompensated} - offset}{slope} \quad (2)$$

where radiance$_{compensated}$ = atmospherically compensated radiance; radiance$_{uncompensated}$ = uncompensated radiance; offset and slope = the fitted line offset (y-intercept) and slope; and all values are a function of wavelength.

(3) We convert the atmospherically compensated spectra to apparent emissivity, which is the ratio of the measured radiance to the blackbody radiance at a reference temperature. Here the reference temperature is the highest brightness temperature in each compensated spectrum over 9.28–13.07 μm. The restricted wavelength range excludes regions with the highest atmospheric interference. Johnson (1998) and Young (1998) give a detailed analysis and error propagation for ISAC applied to SEBASS data.
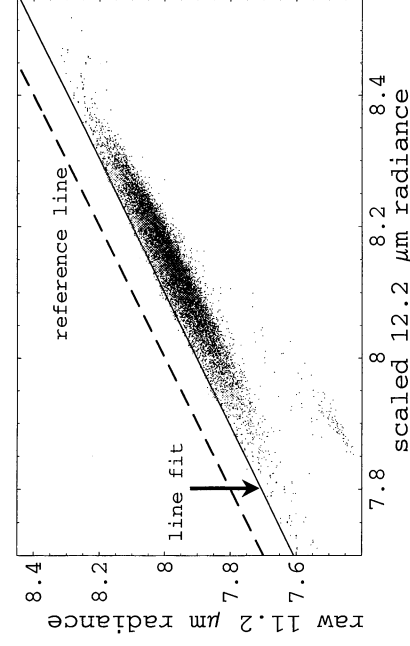
4.2. Field spectrometer

High-quality field spectra covering the same spectral wavelengths as SEBASS were acquired in December 1999, using van-mounted interferometer spectrometers (Fig. 3), a Brunswick Model 21 (M21), and a Block Engineering Model 100 (M100). Field spectrometers have the advantage that they view the target through a shorter atmospheric path length and can focus on specific targets for more in-depth measurements. They also provide a cross-check for the airborne spectra. Table 1 and Flanigan (1996) give instrument details, and Fig. 7 shows the SNR.

Hook and Kahle (1996) and Horton, Johnson, and Lucey (1998) discuss field data reduction, and the field spectra were processed in the following steps.

(1) The Aerospace field spectrometer team converted the interferograms into raw (uncalibrated) spectra using a fast Fourier transform. Spectra measured while staring at a specific target (typically 15–20) are averaged together to increase the SNR.

(2) Blackbody targets were measured periodically for a minimum of five different temperatures over a range from ~288 to 318 K, and calibrated using a second-order polynomial fit to x = raw value and y = blackbody radiance calculated for the target temperature, scaled by the blackbody emissivity.

(3) Measurements of a diffuse (sandblasted) 1 × 1 m aluminum target ($L_{Al\ target}$) were converted to downwelling radiance. The aluminum target was placed next to the geologic target at approximately the same angle of repose, and both were measured within a few seconds of each other to minimize temporal changes. The reflected downwelling radiance is calculated using (Eq. (3)):

$$L_{Al\ target} = (\varepsilon_{target}L_{BB}) + (1 - \varepsilon)L_{down} \quad (3)$$

where ε_{target} = emissivity measured in the laboratory, using hemispherical reflectance converted to emissivity; L_{BB} = blackbody radiance at the target's surface temperature; and L_{down} = downwelling radiance (Fig. 9). The calibration must be extrapolated to cold brightness temperatures for $L_{Al\ target}$, and measurements over a range of calibration target

Fig. 8. Atmospheric compensation for 11.2 μm. The highest brightness temperature in this image most commonly occurs at 12.2 μm, so it is set as the reference radiance. The x-axis shows the 12.2-μm data scaled to the radiance it would exhibit at 11.2 μm at the measured 12.2-μm brightness temperature. The y-axis shows the measured 11.2-μm radiance. The dashed line indicates the radiance for no atmospheric interference (slope=1 and y-intercept=0), and the solid line shows the fit to the maximum points along the scatterplot. The fitted line slope and offset give the atmospheric transmission and upwelling radiance, respectively. Points that are along the fitted line are assumed to have an emissivity of 1 at 11.2 μm, and points below the line an emissivity <1. This calculation is repeated for each wavelength. Radiance units are W/(m^2 sr μm).
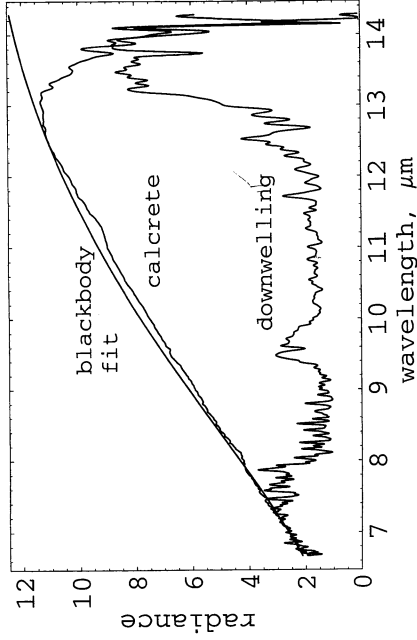
Fig. 9. Field spectrometer measurements. The lower trace shows the downwelling radiance; the middle trace shows the calcite; and the upper trace the blackbody curve for the maximum brightness temperature over 8.10–13.37 μm, which here occurs at 12.52 μm. Radiance units are W/(cm² sr cm⁻¹) that have been multiplied by 10⁶.

effect. Thus, compensation of downwelling radiance will be much more difficult for the strong 9-μm region quartz bands, and less difficult for the 11.2-μm calcrete band.

4.3. Laboratory

Reflectance measurements were made over the 2.5- to 200-μm wavelength regions with a Nicolet Magna 550 Fourier transform infrared (FTIR) spectrometer equipped with a DTGS detector. Biconical reflectance spectra (2.5–200 μm; 4000–50 cm⁻¹) were recorded with a Harrick Scientific "praying mantis" diffuse reflectance attachment. A Labsphere Infragold standard was used as the background spectrum. A solid substrate beamsplitter and DTGS detector with a polyethylene window was used to record spectra from 9 to 200 μm. A region of overlap (9–25 μm) between the coverages of the KBr (2.5–25 μm) and solid substrate beamsplitters allowed spectra from both regions to be scaled if bands existed in the region of overlap. Hemispherical reflectance measurements (2.5–25 μm) were made with a 3-in.-diameter Labsphere integrating sphere lined with Infragold to determine absolute emissivity via Kirchhoff's Law (emissivity=1 − reflectance). The wall of the sphere (with the sample in place) was used to obtain the background spectrum for each sample. The upward-facing weathered sample surfaces (as marked in the field) were examined to better correlate the laboratory spectra with SEBASS data. Relatively flat surfaces were selected for analysis, and when necessary, a water-cooled diamond saw was used to cut appropriately sized specimens from larger samples, with spectra measured of the uncut surface.

In order to identify the major phases present, selected samples were analyzed by X-ray diffraction (XRD) using copper radiation and a computer-controlled Philips Electronics Instruments APD 3720 vertical powder diffractometer. The carbonate contents of samples were determined by gravimetric acid digestion. Hydrochloric acid-insoluble residues were filtered, dried, and weighed to determine the weight percentages of noncarbonate.

The surfaces of the samples (both as weathered and polished cross-sections vacuum impregnated and mounted in epoxy) were examined by scanning electron microscopy (SEM) and chemically characterized by energy-dispersive X-ray spectroscopy (EDXS). After coating with a thin conductive layer of carbon, samples were examined at

temperatures improve this extrapolation. It is preferable to include a cold calibration target measurement, but effects such as icing render this very difficult. We used the ambient temperature as the aluminum target temperature, since it was a very windy and slightly overcast day. To check the effect of this assumption, we varied the assumed aluminum plate temperature, but since the plate emissivity is so low, it was insensitive to this assumption.

(4) Spectra are converted to apparent emissivity (ϵ_A) and compensated for reflected downwelling radiance using the equation:

$$\epsilon_A = \frac{L_{target} - L_{down}}{L_{BB\ surface} - L_{down}} \qquad (4)$$

where L_{target}=measured radiance of the geologic target; $L_{BB\ surface}$=blackbody radiance at the surface temperature, calculated as the highest measured brightness temperature over 8.10–13.37 μm (1235.0–747.9 cm⁻¹) to exclude regions with the highest atmospheric interference (Fig. 9). This method assumes the emissivity at this wavelength is 1. We tested the effect of this assumption on the band depth by using a maximum emissivity of 1 and also 0.96, which is the true maximum emissivity of calcrete over this wavelength range. The difference in band depth is below the noise level.

The relative contribution of the reflected downwelling radiance depends on: (1) the surface material reflectance. The centers of strong bands (reststrahlen bands) are reflectance maxima, and the higher the reflectance, the more the band is affected; (2) the amount of downwelling radiance, which varies with atmospheric temperature, water vapor, and cloud cover; and (3) the relative strength of the surface vs. downwelling radiance. Wavelength regions where the downwelling and surface blackbody curves are relatively close together (see Fig. 9) will have the greatest effect, and at wavelengths less than ~ 8 μm, this effect commonly causes a continuum slope and makes it difficult to extract subtle features. The region from ~ 10 to 12.8 μm will have the least

Table 2
Calcrete and limestone acid residue

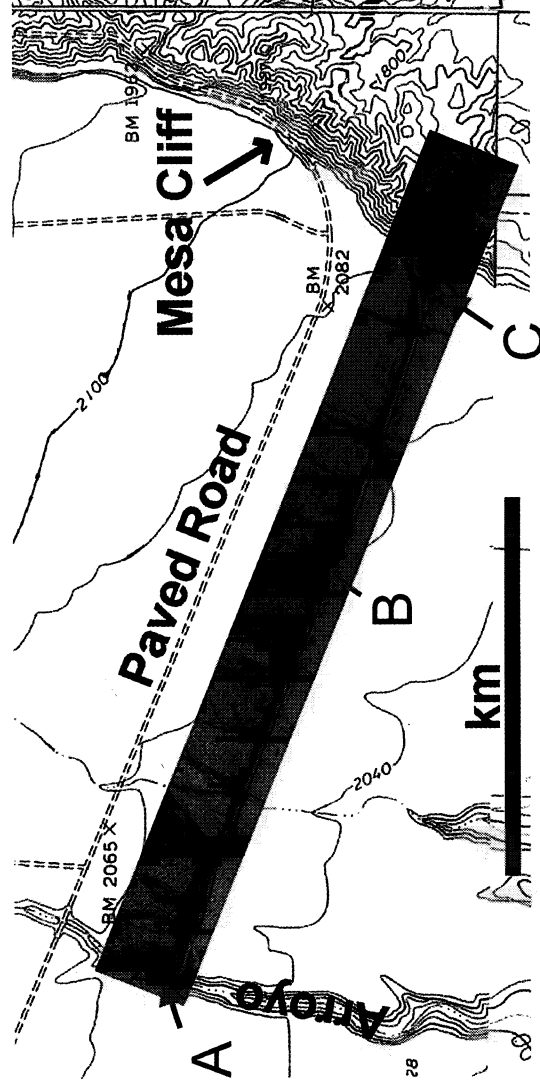| Material	Weight % acid insoluble	Sample
soil/crust	92.6	2–4C
soil/crust	88.1	2–4D
soil/crust	86.3	4–10
calcrete	15.1	2–4B
calcrete	7.9	4–11.5
calcrete	17.0	6–11–1
arroyo limestone	0.5	2–15A

Fig. 10. SEBASS image. This shows a section of a typical SEBASS image overlaid on a topographic map. The SEBASS image was measured directly overlying the labeled road, and is offset for clarity. Red regions have a stronger carbonate band, and blue green regions a stronger quartz band. Arrows mark sample collection regions A, B, and C.

15 kV in an Hitachi S2500 SEM equipped with a KEVEX Delta EDXS system.

5. Sample compositions

Table 2 presents the carbonate contents of the major mesa rock types and soil as determined by gravimetric acid digestion. The XRD pattern of the mesa soil indicated that quartz was the major constituent with minor amounts of calcite (carbonate content 7–14%) and possibly feldspars. In contrast, the calcrete XRD pattern showed that calcite was the major component with minor amounts of quartz and possibly some clays (carbonate content averaging ~87%). The EDXS probes to a depth of about a micron. If the

calcrete surface were covered with clay, the EDXS should record mainly the signature of aluminum and silicon, but this was not observed. The arroyo limestone was nearly pure carbonate (99.5%) and the XRD pattern indicated that it consists primarily of calcite with minor amounts of dolomite.

6. Spectral results and discussion

We used SEBASS images to define spectrally unique regions and examined these in more detail using field spectrometer measurements and laboratory characterization
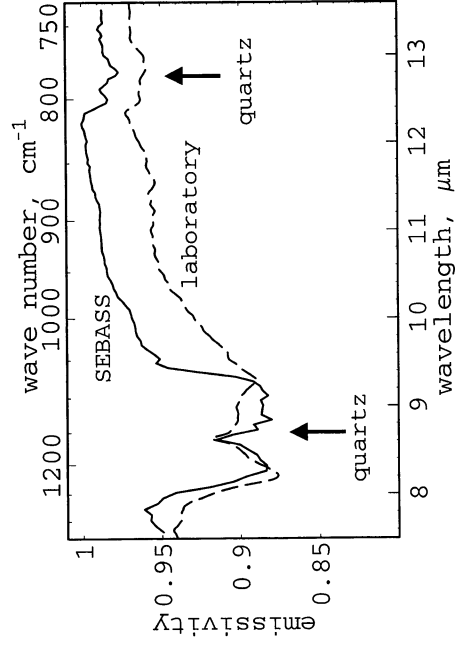

Fig. 11. Soil spectra. The sample was collected near Fig. 10, location "C," and the typical quartz doublets are marked with arrows.
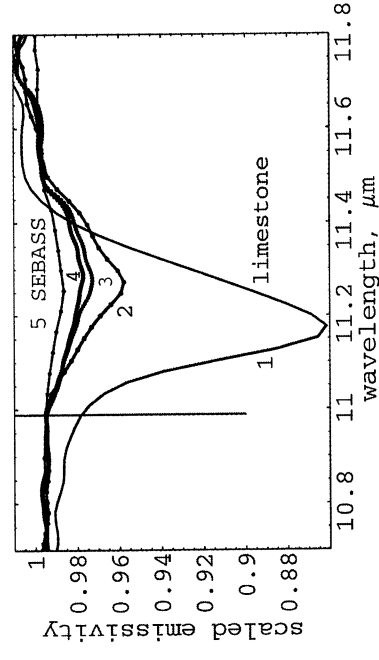

Fig. 15. Calcrete spectra. This shows the laboratory spectra of road limestone (black, trace 1) and typical calcrete (black trace 2), a calcrete field spectrum corrected for reflected downwelling radiance (green, trace 3), the same field spectrum uncorrected for reflected downwelling radiance (blue, trace 4), and the SEBASS spectrum of the same region measured by the field spectrometers (red, trace 5). To allow a more direct comparison, the field and SEBASS spectra have been offset to the same apparent emissivity as the SEBASS spectrum at 10.99 μm (marked with reference line), and the limestone is offset + 0.66.
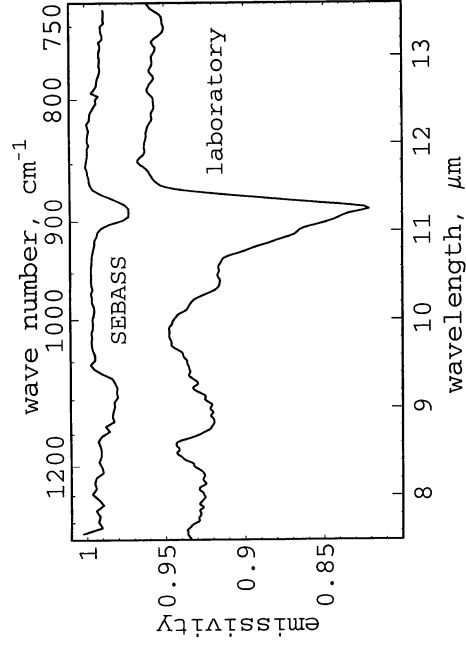
Fig. 12. Arroyo limestone spectra. The SEBASS field of view is only partially filled by the arroyo limestone (Fig. 6) because the target does not consist of 100% limestone. The sample was collected near Fig. 10, location "A."

Fig. 14. Calcrete spectra. At this site, the SEBASS field of view is filled by nearly 100% calcrete. The calcrete surface does not appear rough (e.g., a'a) or vesicular in hand sample. It exhibits a weak but distinct 11.2-μm band. Sample "mm4bhr" was collected near Fig. 10, location "C."

of field samples. We then used the measured spectral contrast to calculate the calcrete detection limit for a range of spectral resolutions.

6.1. SEBASS and laboratory

Since the asphalt road and arroyo conglomerate both contain large limestone fragments (Figs. 5 and 6), they were expected to show a strong 11.25-μm band, and since the topsoil contains only finely particulate calcite, it was expected to exhibit a weak 11.25-μm band. Fig. 10 shows a segment of a typical Mormon Mesa SEBASS image. SEBASS measurements also extended into the valley to the east, but here we focus only on the upper mesa surface. Regions with a strong 9-μm quartz band are shown in blue-green, and regions with a strong 11.25-μm band in red. Red

scales with the apparent emissivity ratio $11.03 \div 11.21$ μm, and blue and green with $9.80 \div 9.06$ μm. Regions that exhibit a strong 11.25-μm band are sections of the asphalt road that have a limestone aggregate and the arroyo conglomerate. Regions covered mainly by calcrete exhibit a weak but distinct 11.25-μm band, and the quartz and calcite topsoil that lack significant calcrete fragments exhibit a weak or undetectable 11.25-μm band.

Field observations and laboratory spectra of hand samples from different locations can be used to explain most of the variations in Fig. 10. In each case, the laboratory spectra are converted from hemispherical reflectance to emissivity using Kirchoff's Law.

Both the airborne and laboratory spectra of soil are dominated by the spectral features of quartz (Fig. 11), as would be expected from the dominant quartz content of all soil samples. The SEBASS spectral curve is slightly offset to higher emissivity than the laboratory spectrum over the 10- to 13-μm range as a consequence of having been matched to a blackbody at 12.2 μm, while the actual emissivity is ~0.98 at that wavelength. Despite this offset and the variable quartz content of the soil, the spectral features agree within expected experimental error. This result demonstrates that under normal conditions, where the target fills the SEBASS field of view, there is excellent agreement between laboratory and SEBASS spectra. Soil samples measured in the laboratory were collected from regions marked in Fig. 10, locations B and C.

Figs. 12 and 13 show SEBASS and laboratory spectra of the arroyo and road limestones. SEBASS recorded the strongest 11-μm band of the road. In both cases, the strong carbonate bands at 11.2-μm seen in the hand specimens are weaker in SEBASS spectra mainly because the limestone covers only a fraction of the surface (Figs. 5 and 6). The arroyo surface is composed mainly of limestone and indurated carbonate. The road is composed mainly of
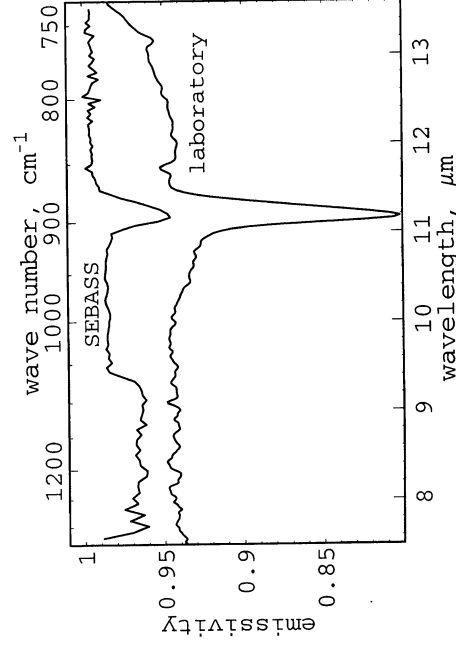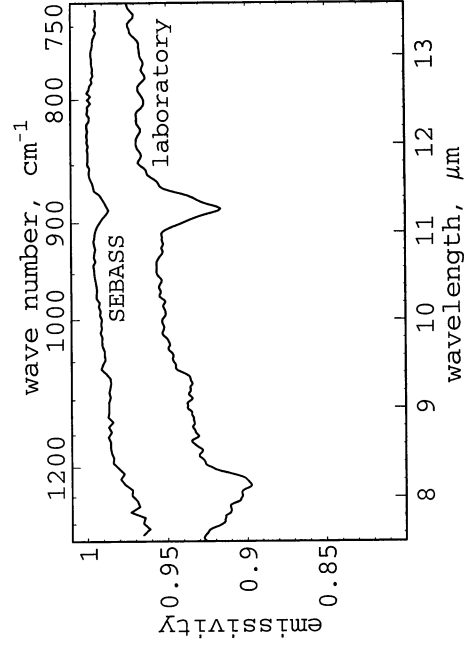

Fig. 13. Road limestone spectra. Silicates in the road aggregate cause the ~9-μm feature in the SEBASS spectrum, while the laboratory spectrum is measured of limestone only. The sample was collected near Fig. 10, location "C."
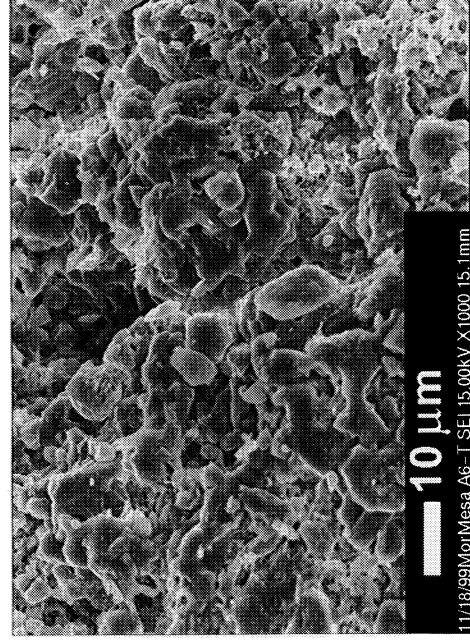
Fig. 16. SEM image of calcrete. Image taken of the upper, weathered surface of a typical calcrete sample. The small, rough grains increase the volume scattering present, and the rough, pitted surface increases the cavity effect.

exposed silicate and limestone aggregate in an asphalt matrix, and silicates introduce the spectral features near 9 μm in Fig. 13.

Fig. 14 shows SEBASS and laboratory spectra of calcrete. Despite the fact that the weathered surface of the massive calcrete appeared relatively smooth (see Fig. 4), laboratory spectra of all hand samples displayed a very weak carbonate band at 11.2 μm, which further laboratory investigation indicated was due primarily to the cavity effect of microscopic roughness not apparent to the eye (see Surface Characterization section). SEBASS spectra also displayed a distinct, but still weaker, carbonate feature, despite having a field of view nearly 100% filled by calcrete at the site selected (near Fig. 10, location C). The feature would be expected to be somewhat weaker because the SEBASS measurements do not remove reflected downwelling radiance, which will reduce spectral contrast. In addi-

tion, laboratory measurements of small (5 mm) areas on hand samples may not fully reproduce field conditions because they do not sample the full range of scale of surface roughness. Thus, field measurements were called for to completely understand this spectral behavior.

6.2. Field spectra

Fig. 15 compares the laboratory limestone (Trace 1) and calcrete (Trace 2) spectra and field spectra of calcrete (Traces 3–5), measured near Fig. 10, location C. Traces 3 and 4 show the field spectrum compensated and not compensated for reflected downwelling radiance, respectively (Eq. (4)). Relative to the scaled emissivity at 10.99 μm, the spectra show ~11.2-μm band contrasts of 0.9% for SEBASS; 1.8% for field 4; 2.2% for field 3; and 3.7% for the laboratory calcrete spectrum.

The change in apparent band depth among laboratory, field, and SEBASS spectra could be explained by differences in the range of scale of surface roughness measured by each. The largest difference, and the one most likely to result in different band contrast, is the difference in spot size between laboratory (5 × 5 mm) and field measurements (~0.3 × 0.3 m). The laboratory measurements do not sample roughness on individual rock surfaces over distances exceeding 5 mm, and, more important perhaps, do not measure the cavity effect of pits and crevices among individual pebbles, cobbles, and boulders. The decrease in band depth between field and SEBASS spectra may also be a matter of the scale of measurement. That is, the SEBASS pixel size (~2 × 2 m) may sample still larger cavities between boulders. Differences in atmospheric compensations applied or the fractional coverage within a pixel may also contribute to the small difference in band depth between field measurements and SEBASS measurements (Fig. 15). The field spectra were measured in areas that exhibited a high 11.2-μm spectral contrast.

6.3. Detection limits

Lower spectral contrast increases the minimum SNR required to detect minerals. Table 3 gives the rms SNR values necessary to detect a 1.5% deep 11.25-μm calcrete band with a band width (Kruse, 1988) of 0.38 μm (30 cm^{-1}).
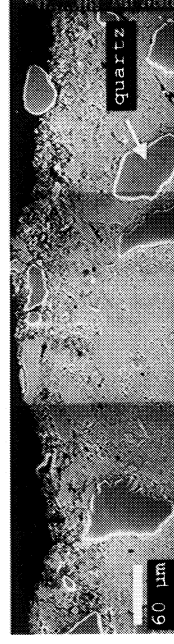

Fig. 17. Calcrete cross-section SEM. This shows an SEM photograph of a polished cross-section of the calcrete surface, which exhibits a rough surface and denser interior. The largest grains are quartz.

Table 3
Minimum SNR for 1.5% 11.2 μm band detection

Sampling interval, (cm^{-1})	Sampling interval, (μm at 11.2 μm)	Minimum rms SNR,[a] 10% coverage[b]	Minimum rms SNR, 69% coverage
2	0.025	1291	215
5	0.063	2041	340
7	0.089	2415	403
10	0.127	2887	481
20	0.253	4082	680
40	0.506	5773	962
80	1.014	8165	1360

[a] The calculation uses peak-to-peak noise, and here we assume the peak-to-peak noise is five times greater than the rms noise (Griffiths and de Haseth, 1986); and a confidence factor of 3 and a band full width at half maximum of 0.38 μm (30 cm^{-1}) (Kirkland et al., 2001).

[b] Percent coverage is the effective aerial exposure by the material (here, calcrete). Effective aerial coverage may be reduced by coatings (e.g., weathering products, desert varnish, dust).
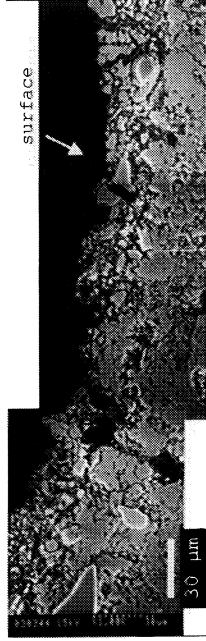
Fig. 20. Road limestone cross-section SEM (close-up). The road limestone surface also has fewer cavities and more flat surfaces than the calcrete.

Fig. 18. Calcrete cross-section SEM (close-up). This a more magnified view than Fig. 17, and illustrates the pitted surface and angular, rough grains.

(Fig. 15) for a range of instrument sampling intervals, where it is assumed the spectral resolution is two times the sampling interval (e.g., the SEBASS sampling interval is 0.044 μm or 3.5 cm^{-1} and the spectral resolution is 0.088 μm or 7 cm^{-1} at 11 μm). Kirkland, Herr, and Salisbury (2001) give details of these calculations. These are the minimum values required for detection, not for identification. The SNR required for detection is proportional to the square root of the number of points measured on the band. Table 3 illustrates the increasing SNR required for detection that occurs as spectral resolution degrades, and shows that at low spectral resolution, the SNR values can become impractical to obtain.

As a result, spectral averaging is commonly used to increase the effective SNR. However, two main issues limit the effectiveness of this approach. First, SNR does not increase without limit with averaging. Second, unless repeated measurements can be made of the same location, the size of the deposit of exposed material required for detection increases, until this approach becomes impractical. To provide a simple illustration of these effects, we assume an example instrument with: (1) SNR that increases linearly with the square root of the number of measurements averaged, and that has no systematic low frequency noise; (2) an rms SNR of 100 and a 0.5-μm (40 cm^{-1}) sampling interval at ~11 μm; and (3) no repeated measurements of the same spatial pixel. The instrument requires an rms SNR of 5773 (Table 3) to detect the calcrete band in a single spectrum for 10% coverage, but it may detect the band if 3333 spectra are averaged. The equivalent linear dimension of the averaged pixel is the linear pixel dimension multiplied by the square root of the number of pixels averaged. Thus, if the instrument measures 10 × 10 m per pixel, then the equivalent averaged pixel size increases to 10 m times the square root of 3333, which is ~580 × 580 m per pixel,

and for 100 × 100 m pixels, the equivalent averaged pixel size is ~5800 × 5800 m.

7. Surface characterization

As indicated in previous sections, microscopic observations of hand samples and field observations of outcrops suggested that the low spectral contrast of the calcrete, despite its relatively smooth appearance, was due primarily to cavity effects in microscopic surface roughness, and secondarily to cavity effects in macroscopic surface roughness. To document the microscopic roughness, the calcrete and limestone surfaces were characterized using SEM. Fig. 16 shows the pitted, rough nature of the calcrete surface. The rough surface will increase the cavity effect, and the small, angular grains will increase the volume scattering, both of which decrease the spectral contrast.

Figs. 17 and 18 show SEM images of a polished cross-section of the calcrete surface, and Figs. 19 and 20 show the arroyo and road limestones, respectively. Fig. 17 shows both the rough, pitted calcrete surface, and also the more dense interior. Gardner (1972) measured calcrete densities ranging from 2.52 to 2.65 g/cm^3, with an average density of 2.62 g/cm^3. Pure calcite crystal has a density of 2.71 g/cm^3, and quartz a density of 2.65 g/cm^3 (Klein & Hurlbut, 1993). Fig. 18 gives a more magnified view of the pitted nature of the calcrete surface. Pits on this scale will cause a cavity effect, even when the calcrete appears to have a fairly smooth surface to the eye (Fig. 4).

The arroyo and road limestone surfaces appear distinctly different from calcrete (Figs. 19 and 20, respectively). They have fewer pits and larger, smoother grains at the surface boundary. Fewer pits reduce the cavity effect, and the larger and smoother surfaces decrease the volume scattering. None of the images shows evidence of a clay coating.

8. Significance

Most statements of detection and identification limits for remotely sensed spectral measurements rely predominantly on laboratory measurements of well-crystalline, smooth-surfaced, pure endmembers. Based on such laboratory studies, it has generally been accepted that a massive carbonate will be both detected and identified by remote
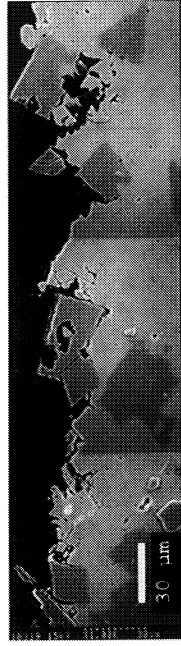

Fig. 19. Arroyo limestone cross-section SEM (close-up). In contrast to the calcrete surface, the arroyo limestone surface has fewer cavities, and more and larger flat surfaces. Darker grains are dolomite.
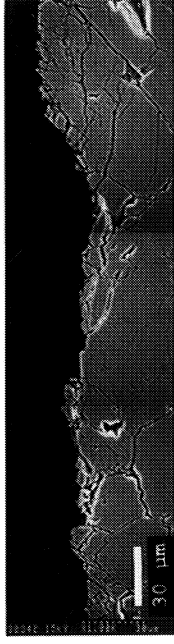
sensing using medium and low SNR spectrometers and even multichannel radiometers.

In light of that, our data illustrate four critical points. First, the calcrete consistently has significantly reduced spectral contrast relative to the limestone, even though both are massive, composed predominantly of calcite, from the same field site, exposed to the same environment, appear reasonably smooth in hand specimens, and measured under exactly the same conditions. Yet, they exhibit remarkably different spectral contrast. Second, field spectra can exhibit a significantly lower spectral contrast than typical laboratory spectra, even when the target material fills the field of view (Figs. 14 and 15). These two points demonstrate the importance of stating the assumed band contrast used to calculate a given detection limit, rather than stating only the composition. Third, field measurements have inherently greater difficulties and thus uncertainties than laboratory spectra. These uncertainties affect the potential mineral detection limit. Fourth, lack of ground truth increases the uncertainties, which again affects the potential detection limit. Ground truth was necessary to finalize an understanding of our measurements, although it is critical to note that ground truth was not necessary to detect and identify the calcrete as a carbonate in the SEBASS spectra. As a result of these effects, detection limits for field spectra will generally fall short of the optimistic expectations based solely on laboratory spectra.

The observed band contrast reduction in the calcrete results mainly from cavities that occur on three scales, from (1) pits between the individual rocks in jumbled piles; (2) rough, pitted rock surfaces at a scale that is visible by eye ($\sim$ mm to cm); and (3) a rough surface at sizes less than $\sim$ 1 mm that can be seen in SEM images (Figs. 16–20) but are not readily detectable by eye. The roughness scale may be comparable to the grain scale and to infrared wavelengths. These cavities cause multiple reflections which increase the continuum emissivity and decrease the band contrast (Eq. (1) and Fig. 1). Laboratory calcrete spectra show that the 6.5- and 33-µm bands also exhibit reduced spectral contrast. Volume scattering from the small, angular particles also causes some of the band contrast reduction, although when this is the dominant cause, it will alter the spectral shape and decrease the continuum emissivity (Fig. 2).

Reduced spectral contrast reduces the sensitivity of any instrument to detecting a material. Nonetheless, SEBASS can both detect and identify the calcrete for $\sim$10% pixel coverage (Table 3). This is the first use of an airborne hyperspectral thermal infrared scanner to identify spectrally subtle material, and it validates the methodology. However, using the 11.2-µm band, a low spectral resolution instrument could not identify the calcrete as a carbonate, and it could detect the band only for measurements made at unusually high SNR (Table 3), or for extensive area deposits to allow abundant averaging, or by using many repeated measurements of the same pixel. For some studies, these differences may be critical, and it shows the contribution made by high SNR and spectral resolution.

These results demonstrate the importance of extending thermal infrared hyperspectral studies from the laboratory to the field. SEBASS supplied the means to find this unexpected spectral behavior because it measures hundreds of thousands of very high SNR, hyperspectral pixels over a more extended spatial region than is possible by collecting field samples and measuring them in the laboratory. It is essential to note that we could not have made this finding using a multiband radiometer. We would not have fully trusted such unusual results without confirmation by the field spectrometer measurements. And finally, we would not have understood the cause of this spectral behavior without the laboratory work.

The results also illustrate the critical importance of exceeding the minimum defined instrument requirements whenever possible. If the objectives include identification of materials that may be weathered and/or rough, then it should be remembered that the field signature of these materials is likely to be weak. This effect should be studied further using field and airborne hyperspectral instruments with sufficient sensitivity and spectral resolution to ensure detection and characterization of unexpected effects that are not reproduced in standard laboratory measurements. These steps are required to ensure instrumentation that will meet the SNR and spectral resolution necessary to detect and identify desired field materials. When interpreting spectral data, it is essential to consider the uncertainties introduced by the possible presence of lower spectral contrast materials, and the possibility that targeted materials may be missed entirely.

Acknowledgments

References

Abrams, M., Abbott, E., & Kahle, A. (1991). Combined use of visible, reflected infrared, and thermal infrared images for mapping Hawaiian lava flows. *Journal of Geophysical Research*, 96, 475–484.

Aronson, J. R., Emslie, A. G., & McLinden, H. G. (1966). Infrared spectra from fine particulate surfaces. *Science*, 152, 345–346.

Barnes, W. L., Pagano, T. S., & Salomonson, V. V. (1998). Prelaunch characteristics of the Moderate Resolution Imaging Spectroradiometer (MODIS) on EOS-AM1. *IEEE Transactions on Geoscience and Remote Sensing*, 36, 1088–1100.

Bartell, F. O. (1981). New design for blackbody simulator cavities. *SPIE Volume, 308: Contemporary Infrared Standards and Calibration*, 22–27.

Christensen, P. R., Bandfield, J. L., Hamilton, V. E., Howard, D. A., Lane,

S. J., Piatek, J. L., Ruff, S. W., & Stefanov, W. L. (2000). A thermal emission spectral library of rock-forming minerals. *Journal of Geophysical Research, 105*, 9735–9739.

Conel, J. E. (1969). Infrared emissivities of silicates: experimental results and a cloudy atmosphere model of spectral emission from condensed particulate mediums. *Journal of Geophysical Research, 74*, 1614–1634.

Crowley, J. K., & Hook, S. J. (1996). Mapping playa evaporite minerals and associated sediments in Death Valley, California, with multispectral thermal infrared images. *Journal of Geophysical Research, 101*, 643–660.

Flanigan, D. F. (1996). A short history of remote sensing of chemical agents. *SPIE Volume, 2763*, 2–17.

Fraden, J. (1993). *AIP handbook of modern sensors* (p. 136). New York: AIP.

Fujisada, H., & Ono, A. (1991). Overview of ASTER design concept. In: P. Slater (Ed.), *Future European and Japanese remote-sensing sensors and programs, Orlando, Florida, April 1–2. Proceedings of the SPIE — The International Society for Optical Engineering*, (vol. 1490, pp. 244–254). Bellingham, WA: Society of Photo-Optical Instrumentation Engineers.

Gardner, L. R. (1968). *The quaternary geology of the Moapa Valley, Clark County, Nevada*, PhD Thesis, Pennsylvania State University.

Gardner, L. R. (1972). Origin of the Mormon Mesa caliche, Clark County, Nevada. *Geological Society of America Bulletin, 83*, 143–156.

Gillespie, A. R. (1992). Enhancement of multispectral thermal infrared images: decorrelation contrast stretching. *Remote Sensing of Environment, 42*, 147–155.

Gillespie, A. R., Kahle, A. B., & Palluconi, F. D. (1984). Mapping alluvial fans in Death Valley, California, using multi channel thermal infrared images. *Geophysical Research Letters, 11*, 1153–1156.

Gillespie, A. R., Kahle, A. B., & Walker, R. E. (1986). Color enhancement of highly correlated images: I. Decorrelation stretch. *Remote Sensing of Environment, 20*, 209–235.

Griffiths, P. R., & de Haseth, J. A. (1986). *Fourier transform infrared spectrometry*. New York: Wiley.

Hackwell, J. A., Warren, D. W., Bongiovi, R. P., Hansel, S. J., Hayhurst, T. L., Mabry, D. J., Sivjee, M. G., & Skinner, J. W. (1996). LWIR/MWIR imaging hyperspectral sensor for airborne and ground-based remote sensing. In: *Imaging spectrometry II. Proceedings of the International Society for Optical Engineering*, vol. 2819, pp. 102–107.

Hook, S. J., Abbott, E. A., Grove, C., Kahle, A. B., & Palluconi, F. (1999). Use of multispectral thermal infrared data in geological studies, Chap. 2. In: A. N. Rencz (Ed.), *Remote sensing for the Earth sciences: manual of remote sensing*, (3rd ed.) vol. 3, pp. 59–110.

Hook, S. J., & Kahle, A. B. (1996). The Micro Fourier Transform Interferometer (µFTIR) — a new field spectrometer for acquisition of infrared data of natural surfaces. *Remote Sensing of Environment, 56*, 172–181.

Horton, K. A., Johnson, J. R., & Lucey, P. G. (1998). Infrared measurements of pristine and disturbed soils: 2. Environmental effects and field data reduction. *Remote Sensing of Environment, 64*, 47–52.

Hunt, G. R., & Logan, L. M. (1972). Variation of single particle mid-infrared emission spectrum with particle size. *Applied Optics, 11*, 142–147.

Hunt, G. R., & Vincent, R. K. (1968). The behavior of spectral features in the infrared emission from particulate surfaces of various grain sizes. *Journal of Geophysical Research, 73*, 6039–6046.

Ingle, J. D. & Crouch, S. T. (1998). *Spectrochemical analysis, Chap. 5*. Englewood Cliffs, NJ: Prentice-Hall.

Johnson, B. R. (1998). In-scene atmospheric compensation: application to the SEBASS data collected at the ARM site, Part 1. *Aerospace Report*, (ATR-99(8407), Part I).

Kahle, A. B., & Alley, R. E. (1992). Separation of temperature and emittance in remotely sensed radiance measurements. *Remote Sensing of Environment, 42*, 107–111.

Kahle, A. B., Gillespie, A. R., Abbott, E. A., Abrams, M. J., Walker, R. E., Hoover, G., & Lockwood, J. P. (1988). Relative dating of Hawaiian lava flows using multispectral thermal infrared images: a new tool for geologic mapping of young volcanic terranes. *Journal of Geophysical Research, 93*, 15239–15251.

Kahle, A. B., & Goetz, A. F. H. (1983). Mineralogic information from a new airborne Thermal Infrared Multispectral Scanner. *Science, 222*, 24–27.

Kahle, A. B., Palluconi, F. D., & Christensen, P. R. (1993). Thermal emission spectroscopy: application to the Earth and Mars, Chap. 5. In: C. Pieters, & P. Englert (Eds.), *Remote geochemical analysis: elemental and mineralogical composition* (pp. 99–120). Cambridge University Press.

Kahle, A. B., & Rowan, L. C. (1980). Evaluation of multispectral middle infrared aircraft images from lithologic mapping in the east Tintic Mountains, Utah. *Geology, 8*, 234–239.

Kaiser, R. D. (1999). Quantitative comparison of temperature/emissivity algorithm performance using SEBASS data. *SPIE Volume, 3717*, 47–57.

King, M. D., & MAS Instrument Team (1996). Airborne scanning spectrometer for remote sensing of cloud, aerosol, water vapor, and surface properties. *Journal of Atmospheric and Oceanic Technology, 13*, 777–794.

Kirkland, L. E., Herr, K. C., & Salisbury, J. W. (2001). Band detection limits in thermal infrared spectra. *Applied Optics, 40*, 4852–4862.

Klein, C., & Hurlbut, C. S. (1993). *Manual of mineralogy* (21st ed.). New York: Wiley.

Kruse, F. A. (1988). Use of Airborne Imaging Spectrometer data to map minerals associated with hydrothermally altered rocks in the northern Grapevine Mountains, Nevada, and California. *Remote Sensing of Environment, 24*, 31–51.

Lane, M. D., & Christensen, P. R. (1997). Thermal infrared emission spectroscopy of anhydrous carbonates. *Journal of Geophysical Research, 102*, 25851–25892.

LaRocca, A. J. (1978). Artificial sources, Chap. 2. In: W. L. Wolfe, & G. J. Zissis (Eds.), *The infrared handbook* (pp. 2–1 to 2–97). Washington, DC: ERIM Press.

Lyon, R. J. P. (1963). Evaluation of infrared spectrophotometry for compositional analysis of lunar and planetary soils. *NASA Technical Note D-1871*.

Lyon, R. J. P. (1964). Evaluation of infrared spectrophotometry for compositional analysis of lunar and planetary soils, Part 2. *NASA Contractor Report 100*.

Nicodemus, F. E. (1965). Directional reflectance and emissivity of an opaque surface. *Applied Optics, 4*, 767–774.

Planck, M. (1914). The theory of heat radiation. *AIP Conference Proceedings*, p. 18 (M. Masius, Trans.).

Ramsey, M. S., & Fink, J. H. (1999). Estimating silicic lava vesicularity with thermal remote sensing: a new technique for volcanic mapping and monitoring. *Bulletin of Volcanology, 61*, 32–39.

Salisbury, J. W., Hapke, B., & Eastes, J. W. (1987). Usefulness of weak bands in mid-infrared remote sensing of particulate planetary surfaces. *Journal of Geophysical Research, 92*, 702–710.

Salisbury, J. W., & Wald, A. (1992). The role of volumes scattering in reducing spectral contrast of reststrahlen bands in spectra of powdered minerals. *Icarus, 96*, 121–128.

Salisbury, J. W., Walter, L. S., Vergo, N., & D'Aria, D. M. (1991). *Infrared (2.1–25 µm) spectra of minerals*. Baltimore: John Hopkins University Press.

Siegel, R., & Howell, J. (1968). Thermal radiation heat transfer. *NASA [Special Publication] SP 164, Vol. 1*.

Vincent, R. K., & Hunt, G. R. (1968). Infrared reflectance from mat surfaces. *Applied Optics, 7*, 53–58.

Vincent, R. K., & Thomson, F. (1972). Spectral composition imaging of silicate rocks. *Journal of Geophysical Research, 77*, 2465–2472.

Vincent, R. K., Thomson, F., & Watson, K. (1972). Recognition of exposed quartz sand and sandstone by two-channel infrared imagery. *Journal of Geophysical Research, 77*, 2473–2477.

Williams, C. S., & Becklund, O. A. (1984). *Optics: a short course for engineers* (pp. 58–63). Malabar: Krieger.

Young, S. J. (1998). Inscene atmospheric compensation: application to the SEBASS data collected at the ARM site, Part II. *Aerospace Report*, (ATR-99(8407), Part II).